Dual-Scale Controls of Vertical Eddy Diffusivity in Tropical Cyclone Rapid Intensification Forecasts

Xuesong Zhu

zhuxs@typhoon.org.cn

Shanghai Typhoon Institute, China Meteorological Administration

Xu Zhang

Shanghai Typhoon Institute, China Meteorological Administration

Bowen Zhao

Shanghai Typhoon Institute, China Meteorological Administration

Wei Huang

Shanghai Typhoon Institute, China Meteorological Administration

Hui Yu

Shanghai Typhoon Institute, China Meteorological Administration

Qijun Huang

Shanghai Typhoon Institute, China Meteorological Administration

Shanghong Wang

Shanghai Typhoon Institute, China Meteorological Administration

Article

Keywords: Tropical Cyclone, rapid intensification, planetary boundary layer scheme, vertical eddy diffusivity, turbulent and mixing process

Posted Date: July 11th, 2025

DOI: https://doi.org/10.21203/rs.3.rs-7052138/v1

Additional Declarations: There is **NO** Competing Interest.

Dual-Scale Controls of Vertical Eddy Diffusivity in Tropical Cyclone Rapid Intensification Forecasts

Xue-Song Zhu[1,2,3*], Xu Zhang[1], Bowen Zhao[1], Wei Huang[1], Hui Yu[1], Qijun Huang[1], and Shanghong Wang[1]

1 Shanghai Typhoon Institute, China Meteorological Administration, Shanghai 200030, China

2 Key Laboratory of Numerical Modeling for Tropical Cyclone, China Meteorological Administration, Shanghai 200030, China

3 Joint Laboratory of Phased Array Weather Radar, Shanghai 200030, China

Submitted to *Nature Geoscience*

* Corresponding author address: Shanghai Typhoon Institute, 166 Puxi Road, Shanghai, 200030, China; Email: zhuxs@typhoon.org.cn

ABSTRACT

The escalating threat of rapidly intensifying Tropical Cyclones (TCs) to global coastal communities underscores the urgent need to advance TC intensity forecasting. While planetary boundary layer (PBL) processes regulate energy sources and sink essential for TC development, improving vertical eddy diffusivity (K_m) parameterization has long been constrained by semi-empirical approaches. Within an unstructured mesh global model framework, we demonstrate that TC rapid intensification (RI) is fundamentally governed by two scaling parameters of K_m: vertical extent (h) and peak magnitude (α), which are optimized through validation against previous observations. Mechanistically, h modulates vortex spin-up efficiency by controlling vertical diffusion and low-level moisture flux gradient, whereas α regulates boundary layer gradient imbalance during RI stage through downward mixing of tangential momentum. Implementation of the optimized K_m parameterization reduces maximum wind speed forecasting error by 58.7% (or 4.5 m s^{-1}) averaged over 72-hour leading time, attributing to the enhanced RI forecasting capability. These findings establish the first unified paradigm linking turbulent processes to RI physics, offering transformative potential for refining TC modeling.

Key Words: Tropical Cyclone, rapid intensification, planetary boundary layer scheme, vertical eddy diffusivity, turbulent and mixing process

1. Introduction

Tropical cyclone (TC) intensity forecasting has lagged behind advances in track prediction in recent decades (DeMaria et al. 2014; Cangialosi et al. 2020). Rapid intensification (RI) occurs when a TC intensifies dramatically over a short period, posing its forecasting challenges due to the unpredictable onset and duration (Emanuel 2017; Emanuel and Zhang 2017). This forecasting gap becomes increasingly critical as observational evidence reveals both accelerated intensification rates of major TCs (Bhatia et al. 2019; Song et al. 2020) and a rising global RI frequency (Zhao et al. 2018; Liu and Chan 2022). Notably, near-coastal RI occurrences have tripled from 1980 to 2020 and may continue to increase under a future warming climate (Li et al. 2023), underscoring an urgent need for improving RI prediction.

The Planetary Boundary layer (PBL) mediates energy exchanges critical for TC intensification, facilitating upward heat and moisture fluxes from the ocean surface while transferring momentum downward through turbulent mixing (Ooyama 1969; Emanuel 1986; Smith and Montgomery 2010). However, these subgrid-scale processes remain inadequately constrained in the vertical eddy diffusivity parameterization within the PBL scheme. As the PBL is conventionally divided into the surface layer and the overlying mixed layer, efforts have been devoted to improving the parameterization of surface fluxes in the surface layer scheme (Powell et al. 2003; Montgomery et al. 2010). In contrast, determining the turbulent momentum and enthalpy fluxes in the mixed layer proves more challenging due to the presence of roll-like vortex structures (Lorsolo et al. 2008). Moreover, turbulence in TC conditions exhibits distinct characteristics from typical convective boundary layer, attributing to the influence of extreme winds and strong inertial stability (Eliassen 1971; Kepert 2001).

Recent progresses in eddy diffusivity parameterization for TC modeling originate from National Oceanic and Atmospheric Administration (NOAA) WP-3D aircraft observations during TC inner-core penetrations. Pioneering work by Zhang et al. (2011) first quantified the vertical momentum flux and corresponding vertical eddy diffusivity for momentum (K_m) in the inflow layers of intense hurricanes Hugo (1989) and Allen (1980). Their findings revealed a positive correlation between K_m and wind speed at 450-m altitude. Subsequent analyses by Zhang and Drennan (2012) extended these observations to four intense hurricanes, providing the first estimates of the vertical distribution of eddy diffusivities. These findings informed

improvements in the K_m formulation to the nonlocal K-profile parametrization (KPP) scheme by introducing an empirical parameter α into the original form of K_m (O'Brien 1970).

$$K_m = ku_* z\left[\alpha\left(1-\frac{z}{h}\right)^2\right], \quad (1)$$

where $k = 0.4$, u_* is the velocity scale, z is the departure from the surface, h is the diagnosed PBL height, and α is the parameter to control the magnitude of K_m. Operational implementation in the operational Hurricane Weather Research and Forecasting (HWRF) model demonstrated that reducing K_m by setting $\alpha = 0.25\text{–}0.5$ yields the best match with the observations (Gopalakrishman et al. 2013; Tallapragada et al. 2014). This reduced K_m results in a shallower PBL and more intense radial inflow (Gopalakrishman et al. 2013; Gopalakrishman et al. 2021), leading to improvements in TC boundary layer structure (Zhang et al. 2015) and intensity forecasts (Zhang et al. 2017), particularly for RI events (Zhang and Rogers 2019). Nevertheless, since the TC vortex may amplify small changes in the boundary layer through nonlinear feedback processes, the extent to which K_m parametrization advances fully explain TC simulation improvements remains unclear.

In addition, the parameterized K_m exhibits strong dependence on the diagnosed PBL height h (Eq. 1), which varies substantially with definition criteria. Analysis of 794 GPS dropsonde profiles within 13 hurricane core regions reveals that the well-mixed layer depth approximates half the inflow layer depth, while Richardson-number-based definitions yield intermediate PBL heights (Zhang et al., 2011). This PBL height sensitivity critically impacts TC forecasts through its influence on the vertical structure of K_m, inflow layer depth, inflow strength, and thereby TC intensity (Kepert 2012). Given that the magnitude parameter (α) and the PBL height scale (h) contribute differently to the parametrized K_m (Eq. 1), their fundamental roles in TC intensification require clarification.

Here we aim to optimize the scaling parameters α and h in the K_m parameterization for TC modeling, ensuring optimal consistency with observational benchmarks from Zhang et al. (2011) and Zhang and Drennan (2012). We will further demonstrate, for the first time to our knowledge, that the dual-scale impacts of K_m on RI are essential but mechanistically distinct, with physical explanations on how parameterized turbulent fluxes govern fundamental RI physics. Finally, we show the implementation potential of the optimized K_m for improving RI

forecasting. The rest of this paper is organized as follows. Section 2 details model configuration and K_m optimization. Section 3 describes the dual-scale controls on RI and the related physical mechanisms. The results and discussions are summarized in section 4.

2. Methods

a. Model setup

The Global-to-Regional Integrated Forecast System (GRIST), an unstructured mesh global model (Zhang et al. 2019, 2020, 2021, 2022; Li et al. 2022, 2023) was originally developed with the purpose to investigate the unified global weather and climate modeling, with flexibly resolution adjustment and multi-physics package configurations. Recently, the GRIST mesoscale weather-climate prediction configuration (GRIST-MWP) has been employed to conduct high-resolution storm-resolving simulations with a global uniform resolution of 3–5 km (Zhang et al. 2022; Huang et al. 2025).

Following our recent research (Huang et al. 2025), we adopt the GRIST-MWP with a variable resolution grid ranging from 4 to 50 km. Figure 1a shows that the finest resolution of 4 km covers most of the western North Pacific and South China Sea, and eastern China, with a rapid transition to 50-km resolution for the rest global domain. Each grid has 31 vertical levels with 5 within the lowest 1.0 km of the model atmosphere. We have utilized the dataset from the National Center for Environmental Prediction Global Forecast System (GFS), which features a resolution of 0.5 degrees. The daily SST is updated from the GFS data. The parameterization schemes used in the control run (CTL1) include the eddy-diffusivity mass-flux (EDMF; Han et al. 2016) PBL scheme, the new version of the rapid radiative transfer model for longwave and shortwave radiation schemes (Iacono et al. 2008), the Tiedkle-Bechtold convective scheme (Bechtold et al. 2008, 2014), Xu-Randall cloud-fraction parameterization (Xu and Randall 1996), and the single-moment 6-class microphysics scheme (Hong et al. 2006).

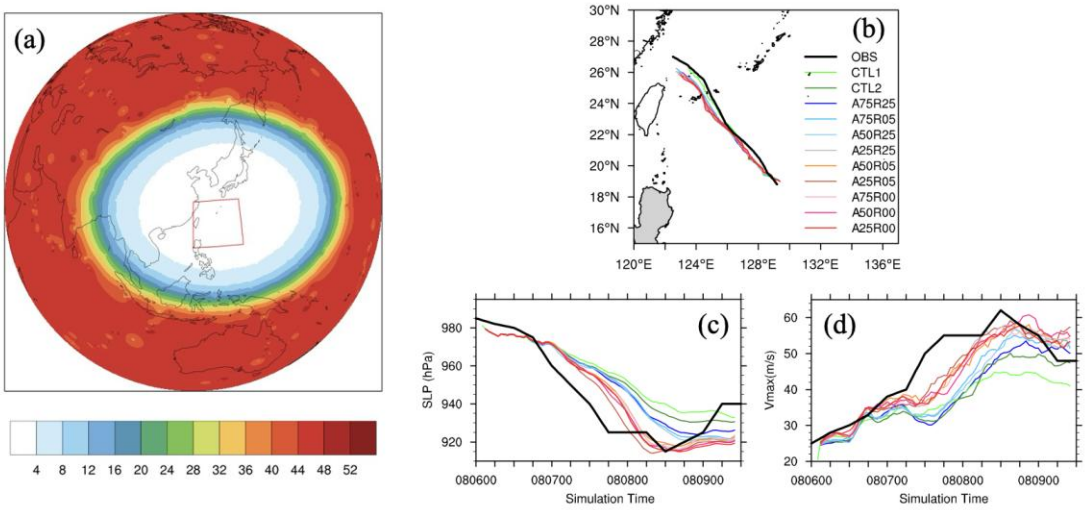

Fig.1. (a) The variable resolution grid adopted in GRIST model, with shading denoting the horizontal resolution ranging from 4 to 50 km. Simulation results within the red box are shown for (b) tracks, (c) minimum sea level pressure (hPa), and (d) 10-m maximum wind speed (m s^{-1}) of Super Typhoon Lekima (2019). The black lines in (b-d) represent the best-track data from China Meteorological Administration, while colored lines are simulation results from numerical experiments as will be described in Table 1.

b. Modifications in EDMF scheme under TC conditions

Two modifications are introduced to the original version of EDMF scheme. Considering the effect of in-cloud mixing above the PBL in improving TC structure and track simulation, the eddy diffusivity (K_m) in the free atmosphere is modified according to our research (Huang et al. 2025). In the original EDMF scheme, the local diffusion scheme (Louis 1979) is utilized for free atmospheric diffusion above the PBL ($z > h$). The eddy diffusivity K_m for momentum and mass above the PBL is defined as:

$$K_m = l^2 f_{m,t}(Rig)\left(\frac{\partial U}{\partial Z}\right) \tag{2}$$

where l is the mixing length, the stability functions $f_{m,t}(Rig)$ are represented by the local gradient Richardson number Rig, and $\frac{\partial U}{\partial Z}$ represents the vertical wind shear.

For the noncloudy layer,

$$Rig = \frac{g}{\theta_v}\left[\frac{\partial \theta_v / \partial z}{(\partial U/\partial z)^2}\right] \tag{3}$$

To include the effect of in-cloud mixing, for the cloudy air, Rig is modified for reduced stability within cloudy air (Durran and Klemp 1982),

$$Rig_c = (1 + \frac{L_v q_v}{R_d T}) \left[Rig - \frac{g^2}{(\partial U/\partial z)^2} \frac{1}{C_p T} \frac{(L_v^2 q_v / C_p R_v T^2 - L_v q_v / R_d T)}{(1 + L_v^2 q_v / C_p R_v T^2)} \right] \quad (4)$$

For cloudy air, Rig in Eq. 3 is replaced by Rig_c in Eq. 4 in computing Eq. 2. This modification of local gradient Richardson number considers the effects of clouds on turbulent mixing through enhancing the diffusivity coefficient.

Additionally, the diagnosed boundary layer height in the original EDMF scheme is defined by the bulk stability between the surface layer and levels above. The bulk Richardson number (Rib) between the surface layer and a level z is defined as:

$$Rib = \frac{g[\theta_v - \theta_s]z}{\theta_{va} U^2} \quad (5)$$

where the θ_v is the virtual potential temperature, and θ_s is the appropriate temperature near the surface. θ_{va} is the virtual potential temperature at the lowest model level, U is the horizontal wind speed.

Given that the definition of PBL height may not work properly in TC conditions (Chen 2022), we use a different PBL height definition that works well in all stability conditions, especially for TC strong winds (Vogelezang and Holtslag 1996). The Richardson number is calculated from the bottom model layer to PBL height h,

$$Rib = \frac{\frac{g}{\theta_{vs}}(\theta_{vh} - \theta'_{vs})(h - z_s)}{(u_h - u_s)^2 + (v_h - v_s)^2 + 100 u_*^2} \quad (6)$$

where z_s is the height of the bottom model level, and u_s and v_s denote zonal and meridional winds at $z = z_s$, respectively. For stable and neutral boundary layers, $\theta'_{vs} = \theta_{vh}$, where θ_{vs} is the virtual potential temperature at $z = z_s$; for unstable conditions, $\theta'_{vs} = \theta_{vs} + \theta_T$ (Troen and Mahrt 1986), where θ_T is virtual temperature excess near the surface. u_* denotes surface frictional velocity.

c. Optimizing the two scaling parameters in K_m

The numerical experiments conducted in this study are summarized in Table 1. CTL2 shares the same configurations with CTL1, except for the use of the modified EDMF in the TC region recognized as the 10-m maximum wind speed no less than 17.2 m s^{-1} and sea level pressure less than 1000 hPa within the finest domain. CTL2 provides the benchmark for experiments 3–

15. Experiments 3–11 are designed with varying parameters α and Rib to produce the best match of K_m with the observations. The sensitivity of the simulated TC intensity to parameters α and Rib is further investaged in experiments 12–15.

Table 1. Numerical experiments design

No.	Experiment	Description
1	CTL1	Original EDMF PBL scheme
2	CTL2	As in CTL1, but switches to the modified EDMF in TC conditions
3	A75R25	As in CTL2, but for α=0.75, Rib=0.25
4	A50R25	As in CTL2, but for α=0.5, Rib=0.25
5	A25R25	As in CTL2, but for α=0.25, Rib=0.25
6	A75R05	As in CTL2, but for α=0.75, Rib=0.05
7	A50R05	As in CTL2, but for α=0.5, Rib=0.05
8	A25R05	As in CTL2, but for α=0.25, Rib=0.05
9	A75R00	As in CTL2, but for α=0.75, Rib=0
10	A50R00	As in CTL2, but for α=0.5, Rib=0
11	A25R00	As in CTL2, but for α =0.25, Rib=0
12	A50R05-A50R25_12h	As in A50R05, but switches to A50R25 since 12h
13	A50R25-A50R05_12h	As in A50R25, but switches to A50R05 since 12h
14	A50R25-A75R25_24h	As in A50R25, but switches to A75R25 since 24h
15	A75R25-A50R25_24h	As in A75R25, but switches to A50R25 since 24h

Figures 1b-d present simulation results for experiments 1–11 in track and intensity of Super Typhoon Lekima (2019). Lekima originated as a tropical storm at 1200 UTC 4 August in the western North Pacific. It subsequently underwent RI, reaching the intensity of a Super Typhoon at 1800 UTC 7 August and achieving its maximum wind speed (MWS) of 62 m s^{-1} at 1200 UTC 8 August. This study focuses on the period between 0000 UTC 6 August and 1200 UTC 9 August. Since the modifications in these experiments are only confined within TC regions, the TC environmental circulations are similar. Consequently, the simulated TC tracks almost overlap (Fig. 1b). In contrast, the simulated intensities are obviously divergent (Figs. 1c,d).

Experiments CTL1, CTL2, A75R25, A75R05, and A50R25, colored in green and blue produce weaker intensities (Figs. 1c,d), whereas the intensities for A25R25, A50R05, A25R05, A75R00, A50R00, and A25R00 shown in warmer colors are significantly improved.

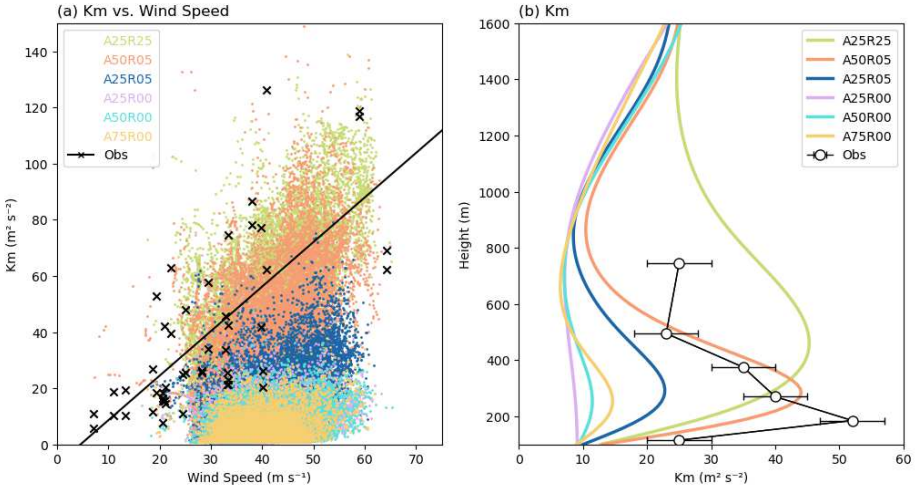

Figure 2. (a) Variations of simulated eddy diffusivity (K_m) with wind speed averaged between 400–500 m heights within the radius of 200 km at 1200 UTC 8 August, compared with observations at 450-m altitude (Zhang et al. 2011). (b) Vertical profiles of the simulated K_m averaged within 200-km radius compared with observations in Zhang and Drennan (2012).

The K_m in the six improved simulations is further evaluated and compared with observations from Zhang et al. (2011) and Zhang and Drennan (2012). Figures 2a depicts the modeled K_m in relation with wind speed averaged at 400-500 m heights, as compared to flight-level (450-m altitude) observations from Hurricanes Hugo and Allen (Zhang et al. 2011). The modeled K_m in A25R05, A25R00, A50R00, and A75R00 is far less diffusive than the observation. Figure. 2b compares the vertical profile of the modeled K_m with estimations in Zhang and Drennan (2012). Clearly, A50R05 with α=0.5 and Rib=0.05 yields a reasonable shape for the vertical profile of K_m within the inner-core region, which matches well with the observation (Fig. 2b). The increasing trend of the observed K_m above 500-m height may imply the mixing effect above the PBL, which is also captured in A50R05 (Fig. 2b). Therefore, the configuration of A50R05 is considered to be the optimized parameterization of K_m in the present study.

3. Dual-Scale controls of K_m in RI

a. Impacts on TC intensity evolution

To examine how the two scaling parameters α and *Rib* influence TC intensification, we compare two pairs of experiments between A50R25 and A50R05, as well as between A75R25 and A50R25 in simulating Typhoon Lekima. The simulated RI and maximum intensity in the optimized configuration of A50R05 is generally closer to the best-track (Figs. 3a,b). In comparison, A75R25 and A50R25 produce the weaker intensities during the simulation time. A clear divergence in MWS emerges between A50R25 and A50R05 around 2000 UTC 6 August, while the intensity evolution remains consistent between A50R25 and A75R25. During this vortex spin-up period, TC slowly decays due to the ocean surface friction (including the diffusion), but spins up as a result of the boundary layer moistening (Smith et al. 2009). This suggests that A50R05 likely experiences either reduced frictional dissipation or enhanced moistening in the boundary layer, compared with the other two experiments. As vortex spin-up continues, a discrepancy in MWS between A50R25 and A75R25 becomes evident near 0900 UTC 7 August, just prior to the simulated RI onset. Meanwhile, the radius of maximum wind (RMW) in A50R05 contracts rapidly at 1000 UTC 7 August to a stagnant radius of 30 km (Fig. 3c). In comparison, RMW in either A50R25 or A75R25 moves inward slowly and maintains at a larger radius when RI occurs (Figs. 3d,e).

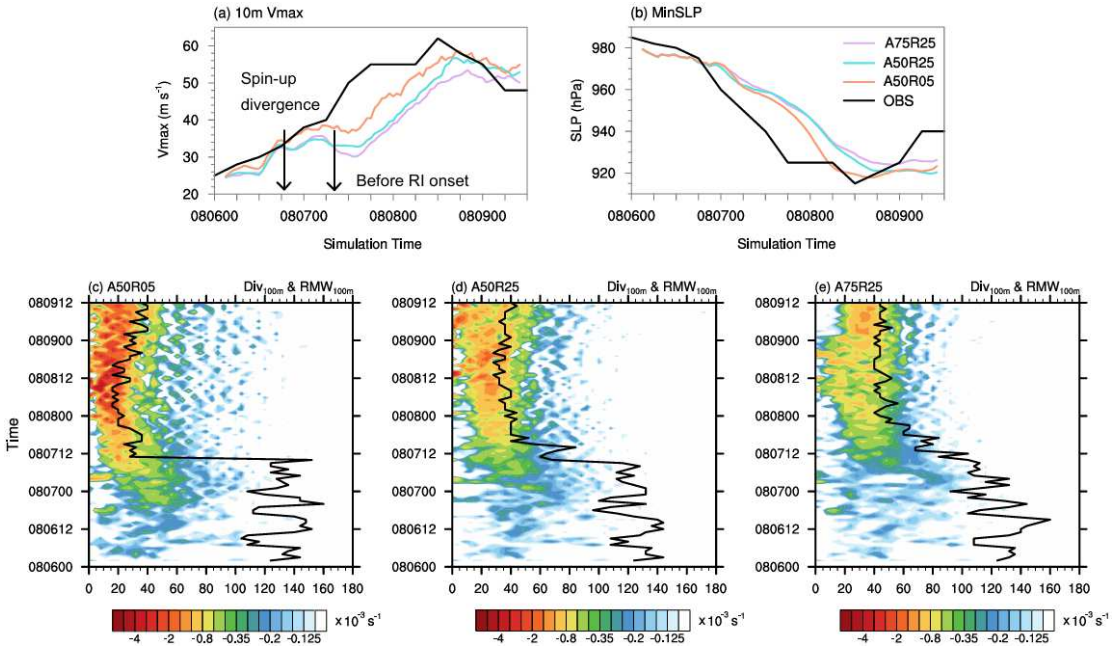

Figure 3. Time evolution of the simulated (a) 10-m maximum wind speed (m s^{-1}) and (b) minimum sea level pressure (hPa) for A50R05, A50R25, and A75R25. Radial-time plot of azimuthal-mean

low-level horizontal convergence (shading; 10^{-3} s^{-1}) and RMW (contour) at 100-m height for (c) A50R05, (d) A50R25, and (e) A75R25.

To investigate the sensitivity of TC intensification to scaling parameters α and Rib, experiments 12–15 are conducted. In experiment 12, we switch Rib=0.05 in A50R05 to Rib=0.25 at 1200 UTC 6 August (denoted as A50R05-A50R25-12h), approximately 8 hours prior to the intensity divergent observed in Fig. 3a. This modification immediately decelerates the MWS growth and elevates the surface level pressure, exhibiting intensity trend analogous to A50R25 (Fig. 4a). Similarly, reversing Rib=0.25 to Rib=0.05 in A50R25 at 1200 UTC 6 August (A50R25-A50R05-12h) produces intensity trajectory largely consistent with A50R05, despite minor discrepancies during 1800 UTC 7 August and 0600 UTC 8 August (Fig. 4b). Besides, simulations with varying parameter α since 00 UTC 7 August in experiments 14 (A50R25-A75R25-24h) and 15 (A75R25-A50R25-24h) show comparable intensity evolution with A75R25 and A50R25, respectively (Figs. 4c,d). These results consistently show that TC intensity changes can be largely explained by changes in parameters Rib and α, suggesting that the two scaling parameters of K_m are the main controlling factors in the simulated TC intensity, with Rib governing the vortex spin-up process while α regulates subsequent RI occurrence.

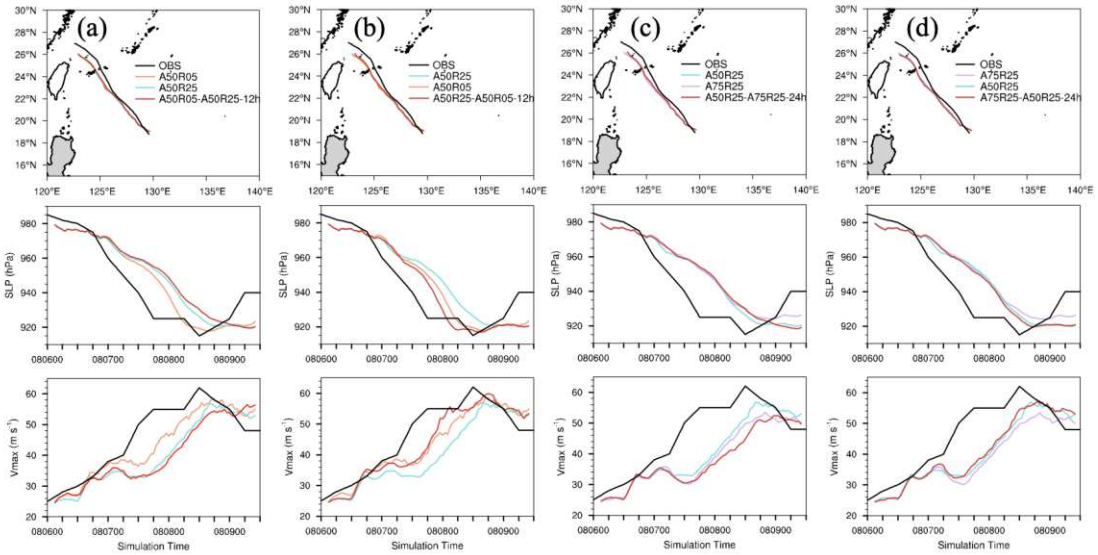

Figure 4. Simulation results of TC track, minimum sea level pressure (hPa), and 10-m maximum wind speed (m s^{-1}) for experiments (a) A50R05-A50R25-12h, (b) A50R25-A50R05-12h, (c) A50R25-A75R25-24h, and (d) A75R25-A50R25-24h.

b. Diffusion and moisture flux gradient during vortex spin-up

To explore why the low-Rib (A50R05) and high-Rib (A50R25) experiments produce divergence, but low-α (A50R25) and high-α (A75R25) show convergence in intensity evolution around 2000 UTC 6 August (Fig. 3a), the roles of the momentum diffusion and moisture fluxes due to K_m are evaluated and compared during the vortex spin-up period.

TC spin-up refers to the acceleration of the mean tangential circulation during initial intensification. Within an axisymmetric framework, the tangential momentum equation in cylindrical coordinates can be expressed as (Montgomery et al. 2020):

$$\frac{\partial \bar{v}}{\partial t} = -\bar{u}\overline{\xi_a} - \bar{w}\frac{\partial \bar{v}}{\partial z} - \overline{u'\xi_a'} - \overline{w'\frac{\partial v'}{\partial z}} + \bar{F}_\lambda, \tag{7}$$

$$F_\lambda = \frac{1}{r^2\rho}\frac{\partial r^2 \rho \tau_{r\lambda}}{\partial z} + \frac{1}{\rho}\frac{\partial \rho \tau_{\lambda z}}{\partial z}, \tag{8}$$

$$\tau_{\lambda z} = K_m\left(\frac{1}{r}\frac{\partial w}{\partial \lambda} + \frac{\partial v}{\partial z}\right), \tag{9}$$

where u, v, and w are radial, tangential, and vertical motion; (r, λ, z) represents the cylindrical coordinates; ξ_a is absolute vertical vorticity; ρ is the air density; F_λ is represented by horizontal and vertical diffusive tendency of tangential momentum as shown in Eq. 8. The overbar denotes the azimuthal mean, and the prime means the deviation from the azimuthal mean. The horizontal diffusion term is ignored because of its much smaller value than other terms. The stress tensor $\tau_{\lambda z}$ in Eq. 8 is expressed as the function of K_m as shown in Eq. 9.

Figure 5 shows tangential wind tendency and its budget terms integrated from every 10-min output during 2000–2200 UTC 6 August. The budget-derived tendency patterns (Figs. 5a2,b2,c2) are basically consistent with direct model outputs (Figs. 5a1,b1,c1), showing positive tendencies in the lower troposphere inside the RMW. The mean radial advection term (Figs. 5a3,b3,c3) dominants the budget, contributing largely to the positive tangential wind tendencies (Figs. 5a1,b1,c1). The diffusion (Figs.5a7,b7,c7) and eddy radial advection (Figs.5a5,b5,c5) terms are negative in the boundary layer and lower troposphere, respectively.

In contrast to high-Rib experiment A50R25 (Fig. 5b7), the negative contribution of vertical diffusion in A50R05 (Fig. 5a7) becomes weaker below the height of 1 km (Fig. 5d7). This weaker diffusion, together with the weaker eddy radial advection (Fig. 5d5) facilitates the positive value in the budget difference (Fig. 5d2), and thus can explain the faster tangential wind acceleration outside the radius of 100 km in the low-Rib experiment (Fig. 5d1). Comparing between the low-α (A50R25) and high-α (A75R25) experiments, the vertical diffusion terms are nearly identical (Fig. 5e7) at the beginning of spin-up period, when the horizontal wind is relative weak (30–40 m s^{-1}). This results in a comparable budget around the RMW (Fig. 5e2) and therefore an equal tangential wind tendency (Fig. 5e1).

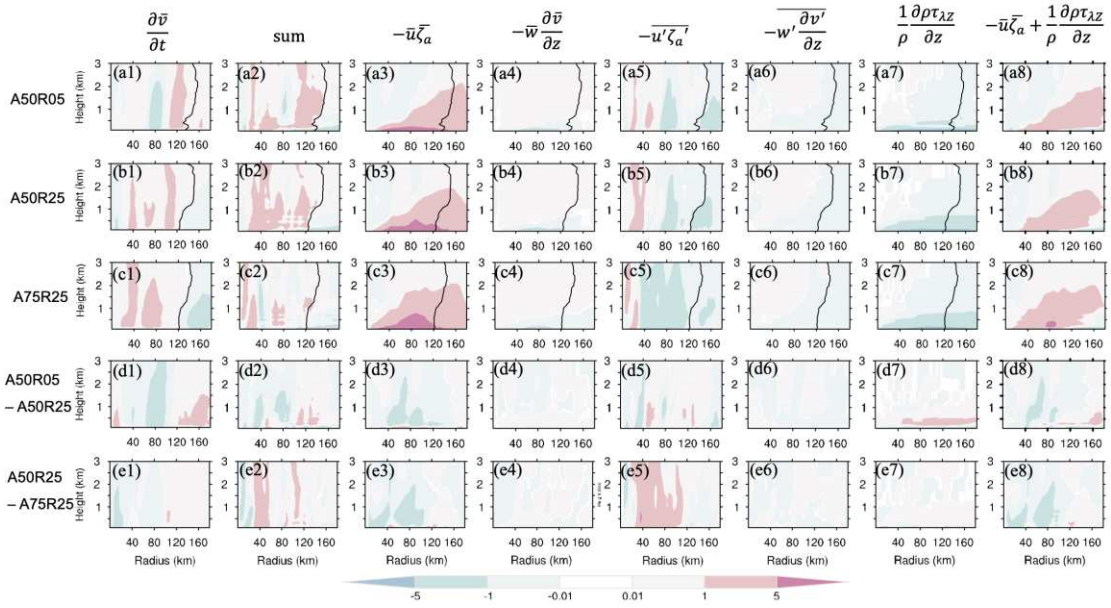

Fig. 5. (a1) Hourly change in the azimuthal-mean tangential wind (shaded; m s^{-1} h^{-1}) and (a2) the sum of the tangential wind budget (shaded; m s^{-1} h^{-1}) averaged over 2000–2200 UTC 6 August for A50R05. The individual budget terms (shaded; m s^{-1} h^{-1}) are (a3) mean radial advection, (a4) mean vertical advection, (a5) eddy radial advection, (a6) eddy vertical advection, and (a7) vertical diffusion. (a8) sum of mean radial advection and vertical diffusion. (b1–b8) and (c1-c8) As in (a1–a8), but for A50R25 and A75R25. (d1–d8) and (e1-e8) are differences between (a1-a8) and (b1-b8), and (b1-b8) and (c1-c8), respectively. Black contour shows the location of RMW.

Consistent with the K_m profile (Fig. 2b), the subgrid-scale moisture flux in A50R05 is generally weaker within the boundary layer and decreases more rapidly in the lower 300-m

altitude (Fig. 6a). This rapidly weaking of moisture flux implies that less moisture is transferred upward to higher layers and thus more is left within the bottom of the boundary layer. Consequently, the moistening tendency generated by PBL scheme is more pronounced within the lower 300-m height in A50R05 (Figure not shown), contributing to a moister inner-core environment within the lower boundary layer in low-Rib experiment (Fig. 6b). Time evolution of low-level moisture flux gradient between 100–200 m heights and specific humidity at 100-m height averaged within 200-km radius are shown in Figs. 6c,d. Notably, the subgrid moisture flux gradient is more evident in A50R05 (Fig. 6c). As the gradient strengthens since 1200 UTC 6 August and peaks around 0600 UTC 7 August (Fig. 6c), the low-level specific humidity increases more dramatically than in A50R25 and A75R25 (Fig. 6d). This is consistent with the MWS evolution as shown in Fig. 2a, highlighting the linkage between near-surface humidity and TC intensity during vortex spin-up stage.

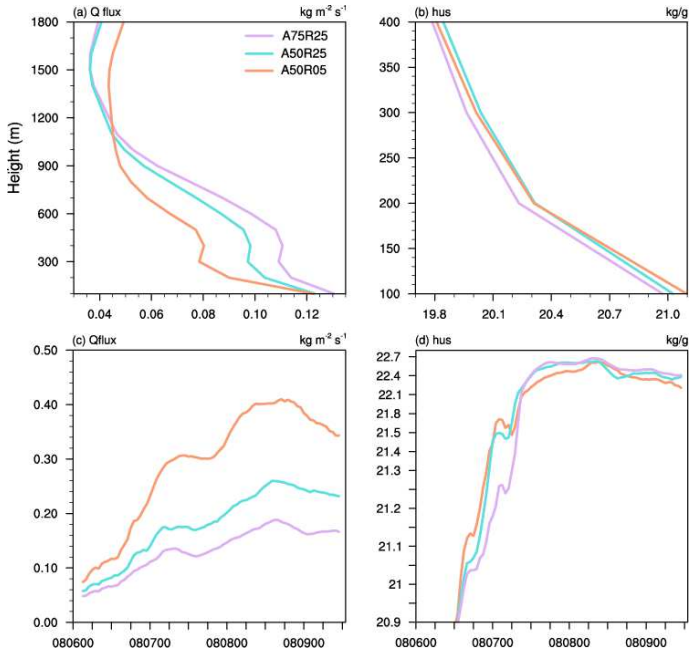

Figure 6. Vertical profile of azimuthal-mean (a) subgrid-scale moisture flux (kg m^{-2} s^{-1}), and (b) specific humidity (10^{3} kg kg^{-1}) at 2000 UTC 6 August within 200-km radius from TC center for A50R05, A50R25, and A75R25. Time evolution of (c) moisture flux gradient within the lower 200 m levels and (d) 200-m height specific humidity averaged within the radius of 200 km for A50R05, A50R25, and A75R25.

Considering the above, the reduced vertical extent of eddy diffusivity contributes to the suppressed momentum diffusion and enhanced moisture flux gradient. This, in turn, results in the stronger tangential wind tendency and moister near-surface environment. This scenario meets the assumption of the evaporation-wind intensification mechanism, known as wind-induced surface heat exchange (WISHE). WISHE proposes a positive feedback between the increase of the near-surface mixing ratio in the core region, an enhanced radial gradient of equivalent potential temperature throughout the boundary layer, and the axisymmetric tangential wind acceleration (Emanuel 1986, 2003; Montgomery and Smith 2014).

c. Boundary layer imbalance during RI onset

To gain insights into the impact of the parameter α on TC intensification around RI onset, we conduct a comparative analysis of downward momentum mixing and its role in the development of the secondary circulation between A50R25 and A75R25. The net radial forcing (NRF) is defined as the sum of the Corios force, the centrifugal force, and the radial component of pressure gradient force (Smith et al. 2009):

$$NRF = fv + \frac{v^2}{r} - \frac{1}{\rho}\frac{\partial p}{\partial r} \tag{10}$$

where f is the Coriolis parameter, and p is air pressure. Note that if $NRF = 0$, the tangential flow is in gradient wind balance; if $NRF < 0$, it is supergradient wind, and if $NRF > 0$, the flow is subgradient. An air parcel will undergo a radially inward acceleration when the NRF is negative or radially outward acceleration if the NRF is positive. Thus, the NRF governs the radial flow and hence the secondary circulation.

Figure 7 illustrates the azimuthally averaged eddy diffusivity, radial and tangential flows, along with the NRF during the initial (Figs. 7a,b) and mature (Figs. 7d,e) RI stages. The eddy diffusivity within the boundary layer has a maximum of 60–80 $m^2\ s^{-1}$ for A50R25 (Figs. 7b,e), compared to 80–100 $m^2\ s^{-1}$ for A75R25 (Figs. 7a,d). These eddy diffusivity maxima locate around the radii where the maximum tangential winds appear. Beneath these diffusivity maxima, a negative NRF is found within the lower boundary layer, where the radial inflow is accelerated. Travelling inward, the radial flow decelerates because the NRF turns to be positive around the radius of 40 km. Consequently, an outflow that relates to the supergradient wind is observed at the top of the boundary layer, just above the positive NRF core. In contrast to A75R25, A50R25

exhibits a stronger subgradient (supergradient) flow, resulting in a stronger radial inflow (outflow) and a stronger secondary circulation (Figs. 7c,f). The results are consistent with previous studies, which indicated that reducing α in the boundary layer parameterization causes enhanced boundary layer inflow, stronger secondary circulation, and stronger convergence closer to the TC center (Zhang et al. 2017). Interestingly, the tangential velocity core in A50R25 (Figs. 7b,e) occupies a shorter vertical extent than that in A75R25 (Figs. 7a,d), although the maximum tangential velocities are comparable between them. As a result, a negative difference in tangential wind is evident both above and at the bottom of the boundary layer, coinciding with the negative NRF difference (Figs. 7c,f).

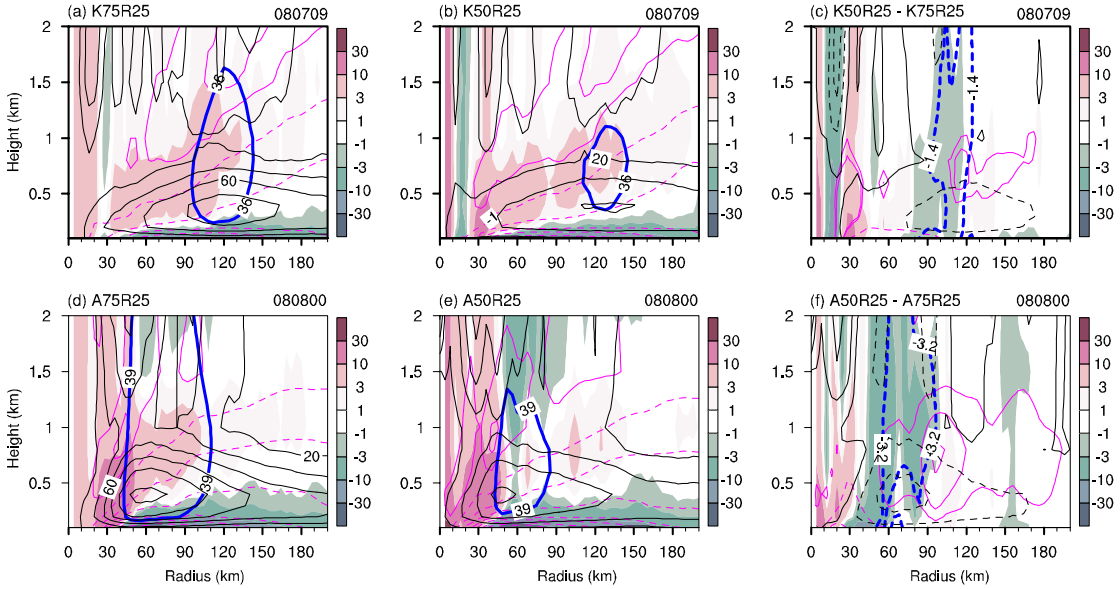

Figure 7. Radial-height plot of azimuthal-mean eddy diffusivity (black contour interval 20 m^2 s^{-1}), the radial inflow (pink dashed contour interval 2 m s^{-1}; –11 to –1 m s^{-1}) and outflow (pink solid contour interval 0.5 m s^{-1}; 0.5 to 2 m s^{-1},), tangential wind core (blue contour; m s^{-1}), and the net radial force (shading; m s^{-1} h^{-1}) at 0900 UTC 7 August for (a) A75R25, (b) A50R25, and (c) the difference between A50R25 and A75R25; (d–f) As in (a–c), but for 0000 UTC 8 August.

To illustrate the connection between the reduction of α and the enhanced boundary layer subgradient flow during RI period (Figs. 7c,f), we explore the origin of the subgradient flow in the boundary layer. Since NRF is determined by the inward-pointing pressure gradient force ($-\frac{1}{\rho}\frac{\partial p}{\partial r}$) and the outward Coriolis and centrifugal forces ($fv+\frac{v^2}{r}$), we calculate these terms at

100-m height, averaged within 0.5–1.0 RMW, where the negative NRF difference is obvious (Figs. 7c,f). The calculation results during 0600 UTC 7 August and 0200 UTC 8 August for A75R25 and A50R25 are shown in Figs. 8a,b, respectively. Given the increasing trend of the positive Coriolis and centrifugal terms, the negative NRF continues to decrease during the simulation time. This implies the dominant role of the radial pressure gradient force in generating the negative NRF for A75R25 and A50R25 (Figs. 8a,b). Additionally, we compare these terms between the two experiments in Fig. 8c. It shows that the radial pressure gradients of the two experiments are approximately equal, as their difference varies around zero during this period. This can be explained by the comparable tangential velocities at the top of the boundary layer as indicated in Figs. 7c,f. However, the difference in NRF becomes obvious towards the mature stage of RI, sharing the similar tendency as that of the sum of the Coriolis and centrifugal forces (Fig. 8c). This means that in comparison with A75R25, A50R25 produces the stronger subgradient due to the reduced Coriolis and centrifugal forces, which further results from the weaker tangential winds (Figs. 7c,f, and 8c).

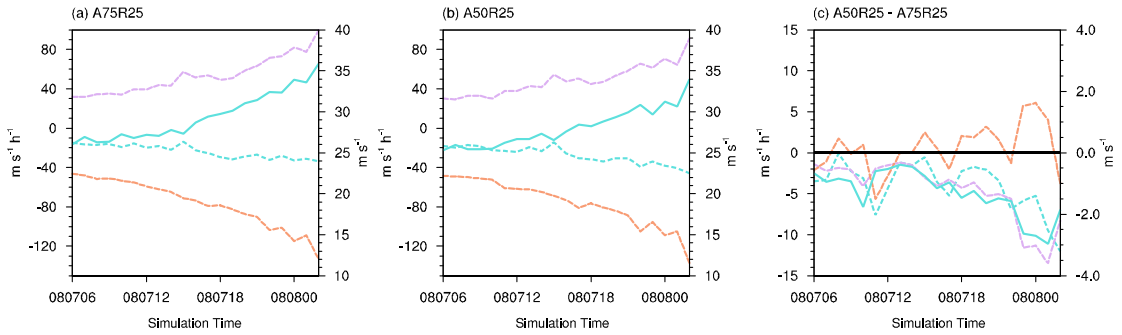

Figure 8. Evolution of azimuthal-mean radial pressure gradient force (orange; m s^{-1} h^{-1}), sum of the outward Coriolis and centrifugal forces (purple; m s^{-1} h^{-1}), the net radial force (dashed green; m s^{-1} h^{-1}), and tangential velocity (green; right coordinates; m s^{-1}), radially averaged within the 0.5–1.0 RMW for (a) A75R25, (b) A50R25, and (c) the difference between A50R25 and A75R25.

Therefore, a larger α induces a larger vertical gradient of eddy diffusion, which more efficiently mixes azimuthal momentum down to the surface, enhancing the low-level tangential wind (Figs. 7c,f), and thereby strengthening the outward Coriolis and centrifugal forces in the lower boundary layer (Fig. 8c). On the contrary, a reduced α leads to weaker tangential wind

and weaker outward Coriolis and centrifugal forces (Figs. 7c,f), and thus a larger gradient wind imbalance in the lower boundary layer. This stronger imbalance, in turn, drives stronger inflow and strengthens the overturning circulation in the inner core. Previous studies (Gopalakrishnan et al. 2013; Gopalakrishnan et al. 2021) considered that larger (smaller) diffusion has a deeper (shallower) boundary layer and negates (enhances) the gradients between the surface layer and the PBL, and therefore leads to weaker (stronger) frictional forces and weaker (stronger) inflow. Here we raises a new pathway by which the peak magnitude of vertical diffusivity influences boundary layer unbalanced dynamics and intensification process under identical PBL height condition.

d. Implementation on RI events

To evaluation the performance of the optimized K_m parameterization (A50R05) in TC forecasting, simulations of five additional TCs over the western North Pacific are conducted and compared between configurations with the CTL1 and A50R05 (see Table 1). These TC cases include Super Typhoons Soudelor (2015), Hato (2017), and Doksuri (2023), as well as Strong Typhoons Hagupit (2020) and In-fa (2021). Note that these cases are chosen due to the poor performance of the control run (CTL1) in TC intensity simulation (Fig. 9). Clearly, CTL1 fails to capture the RI trends for Soudelor (Fig. 9), Doksuri (Fig. 9), and Lekima (Fig. 1). Additionally, discrepancies exist between the simulated intensity and best-track for Hato (Fig. 9b) and Hagupit (Fig. 9c). For In-fa, the CTL1 simulated intensity is weaker initially but stronger later (Fig. 9d). In comparison, A50R05 substantially improves the simulated TC intensities, particularly during RI periods for Soudelor (Fig. 9a) and Doksuri (Fig. 9e). The simulated intensity during the weaking stage of In-fa is more consistent with the observation (Fig. 9d). however, simulated intensities for Hato (Fig. 9b) and Hagupit (Fig. 9c) show limited improvement, possibly due to the inadequate progress in track simulations.

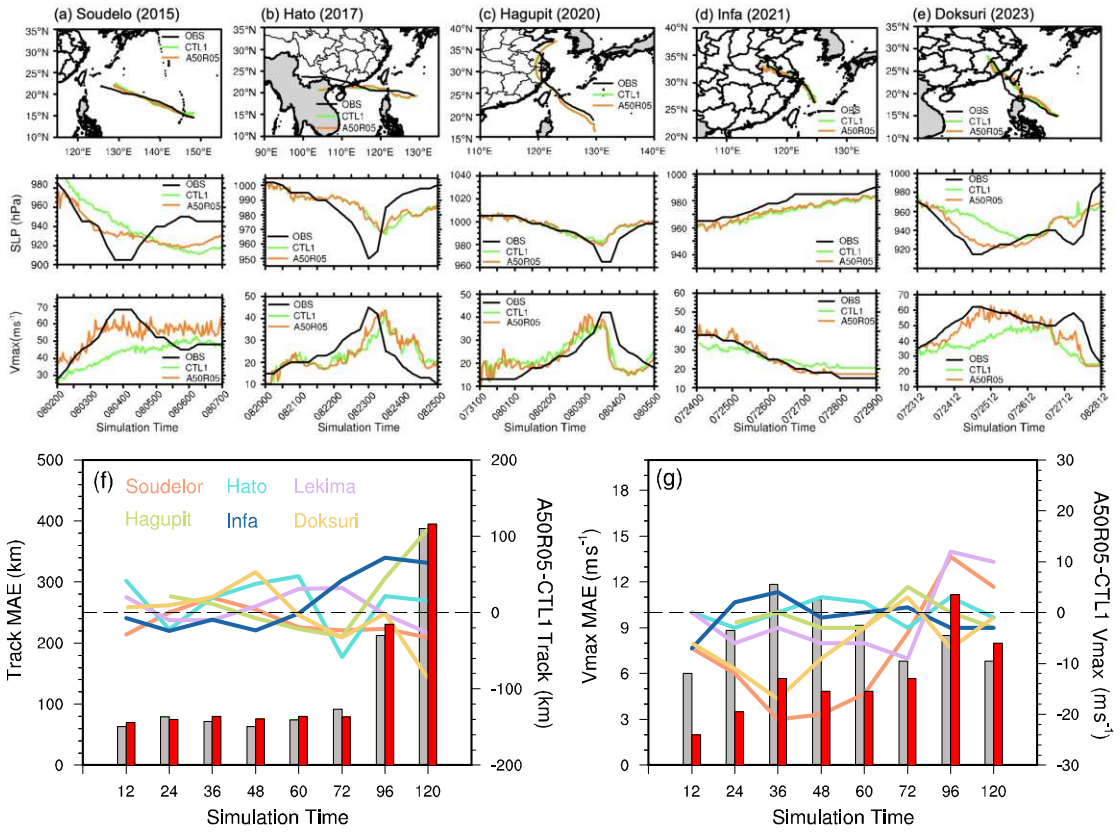

Figure 9. The track, minimum sea level pressure and 10-m maximum wind in experiments CTL1 and A50R05, compared with the best-track from China Meteorological Administration for Typhoons (a) Soudelor, (b) Hato, (c) Hagupit, (d) In–fa, and (e) Doksuri. Absolute errors composited by six typical TC cases at given time interval for experiments CTL1 (gray bar) and A50R05 (red bar), and relative errors for each TC between A50R05 and CTL1 in (f) track (km) and (g) maximum wind speed (m s^{-1}). Note that Typhoon Hagupit was recorded in the best track 24 h after the initiation of the simulation. Thus, the errors at 12 h are not included here.

Absolute errors of the simulated tracks and intensities are composed for the six TC cases and presented at specific time intervals in Figs. 9f,g, accompanied by relative errors between A50R05 and CTL1 for each TC. A negative relative error indicates reduction absolute error or improved simulation, while a positive value denotes deterioration. As shown in Fig.9f, the simulated tracks are rarely improved in A50R05. Absolute track errors remain comparable to those in CTL1, ranging from 80 to 95 km prior to 72-hour, but significantly increase to 200 and 400 km over the subsequent two days. Notably, composite intensity errors are significantly reduced by 58.7% (or 4.5 m s^{-1}) averaged within 72-hour in the simulation time (Fig. 9g).

Consistent with results in Figs. 9a-e, this reduction in intensity error is primarily attributed to the improved RI simulations for Typhoons Soudelor, Lekima, and Doksuri, as indicated by their negative relative errors (Fig. 9g).

5. Summary and discussion

We have proposed an improved eddy diffusivity (K_m) parameterization for the eddy-diffusivity mass-flux (EDMF) scheme considering Tropical Cylone (TC) conditions. Based on the observational constraints from Zhang et al. (2011) and Zhang and Drennan (2012), we optimize two scaling parameters in association with the vertical extent (h) and peak magnitude (α) of the modeled K_m. Further examination reveals that the dual-scale controls of K_m play essential and distinct roles in TC rapid intensification (RI).

The vertical extent scale h determines the early vortex spin-up through momentum diffusion and moisture flux processes. Dynamically, a decrease in h leads to the reduced diffusion and hence the faster tangential wind acceleration. Thermodynamically, more moisture is retained within the bottom of the boundary layer due to the rapid weakening of moisture flux with height in the reduced h. Consequently, the increased near-surface moisture and the enhanced tangential wind may cooperate in the similar way as the positive feedback process in the wind-induced surface heat exchange (WISHE) intensification mechanism.

The magnitude scale parameter α modulates the gradient imbalance within the boundary layer and hence the secondary circulation during RI onset by downward momentum mixing. As the axisymmetric tangential winds accelerate at the top of the TC boundary layer due to the gradient wind balance dynamics, the eddy diffusivity mixes azimuthal momentum down to the surface, thereby enhancing the outward Coriolis and centrifugal forces. Consequently, the gradient imbalance between the Coriolis, centrifugal, and the radially inward pressure gradient forces is reduced. Therefore, a reduced α leads to a smaller increase in tangential wind near surface, and hence the larger gradient imbalance. The resulting stronger radial acceleration and stronger secondary circulation in the reduced α account for a faster and earlier contraction of the radius of maximum wind during RI period.

To our knowledge, the present study presents a first look into key process in association with the parameterized K_m leading to RI of a TC. We believe that the results are also important

for providing a framework for further improving parameterization schemes. It should be noted that more computing resources are still needed to test the robustness of the results with more TC cases. This is a topic for future studies.

Acknowledgments. This research has been jointly supported by the National Key R&D Program of China (2024YFB3910005, 2021YFC3000805), the National Natural Science Foundation of China (4247051181, U2142206, U2342203), and Research Program from Science and Technology Committee of Shanghai (22ZR1476500, 24ZR1479800, 23DZ1204700, 24YF2756900).

Author contributions. Xue-Song Zhu conceived the study and analyzed the initial results. Xu Zhang analyzed the subgrid-scale parameterization. Bowen Zhao contributed to the mapping and calculating. Wei Huang and Hui Yu prepared the modeling framework. Qijun Huang and Shanghong Wang discussed the TC intensification process.

Data availability statement. The numerical model simulations upon which this study were based are too large to archive or to transfer. Instead, the datasets are available from Xue-Song Zhu (zhuxs@typhoon.org.cn) upon request. The TC best-track data in this study was provided from China Meteorological Administration and can be downloaded from https://tcdata.typhoon.org.cn/zjljsjj.html. GFS data was downloaded from https://rda.ucar.edu/datasets/d084001/.

Code available stagement. The code for the analysis and mapping used in this study is available via Zenodo (https://zenodo.org/records/15812533).

Reference

Bechtold, P., M. Köhler, T. Jung, D.-R. Francisco, L. Martin, J. R. Mark, V. Frederic, and B. Gianpaolo, 2008: Advances in simulating atmospheric variability with the ECMWF model: From synoptic to decadal time-scales. Quart. J. Roy. Meteor. Soc., 134(634): 1337–1351, https://doi.org/10.1002/qj.289.

505 Bechtold, P., N. Semane, P. Lopez, J. P. Chaboureau, and N. Bormann, 2014: Representing
506 equilibrium and nonequilibrium convection in large-scale models. J. Atmos. Sci., 71(2): 734–
507 753, https://doi.org/10.1175/JAS-D-13-0163.1.
508 Bhatia, K. T., G. A. Vecchi, T. R. Knutson, H. Murakami, C. E. Whitlock, 2019: Recent increases
509 in tropical cyclone intensification rates. Nat. Commun. 10, 635,
510 https://doi.org/10.1038/s41467-019-08963-y.
511 Cangialosi, J. P. , E. Blake, M. Demaria, A. Penny, A. Latto, and E. Rappaport, and V. Tallapragada,
512 2020: Recent progress in tropical cyclone intensity forecasting at the national hurricane center.
513 Weather and Forecasting, 35(5), 1913-1922, https://doi.org/10.1175/WAF-D-20-0059.1.
514 Chen, X. (2022). How do planetary boundary layer schemes perform in hurricane conditions: A
515 comparison with large-eddy simulations. J. Adv. Model. Earth Syst., 14, e2022MS003088,
516 https://doi.org/10.1029/2022MS003088.
517 DeMaria, M., C. R. Sampson, J. A. Knaff, and K. D. Musgrave, 2014: Is tropical cyclone intensity
518 guidance improving? Bull. Am. Meteorol. Soc. 95, 387–398 (2014),
519 https://doi.org/10.1175/BAMS-D-12-00240.1.
520 Durran, D.R., J. B. Klemp, 1982: The effects of moisture on trapped mountain lee waves. J. Atmos.
521 Sci. 39, 2490–2506. https://doi.org/10.1175/1520-0469(1982)039<2490:TEOMOT>2.0.CO;2.
522 Eliassen, A., 1971: On the Ekman layer in a circular vortex. J. Meteor. Soc. Japan, 49, 784–789,
523 https://doi.org/10.2151/jmsj1965.49A.0_784.
524 Emanuel, K., 1986: An air-sea interaction theory for tropical cyclones. Part I: Steady state
525 maintenance. J. Atmos. Sci., 43, 585–604, https://doi.org/10.1175/1520-
526 0469(1986)043<0585:aasitf>2.0.co;2.
527 Emanuel, K., 2003: Tropical cyclones. Annu. Rev. Earth Planet. Sci., 31, 75–104,
528 https://doi.org/10.1146/annurev.earth.31.100901.141259.
529 Emanuel, K., 2017: Will global warming make hurricane forecasting more difficult? Bull. Am.
530 Meteorol. Soc. 98, 495–501, https://doi.org/10.1175/BAMS-D-16-0134.1
531 Emanuel, K., and F. Zhang, 2017: The role of inner-core moisture in tropical cyclone predictability
532 and practical forecast skill. J. Atmos. Sci. 74, 2315–2324, https://doi.org/10.1175/JAS-D-17-
533 0008.1.

Gopalakrishnan, S., A. Hazelton, and J. A. Zhang, 2021: Improving hurricane boundary layer parameterization scheme based on observations. Earth and Space Science, 8, e2020EA001422. https://doi.org/10.1029/2020EA001422.

Gopalakrishnan, S., F. Marks, J. A. Zhang, X. Zhang, J.-W. Bao, and V. Tallapragada, 2013: A study of the impacts of vertical diffusion on the structure and intensity of tropical cyclones using the high resolution HWRF system. J. Atmos. Sci., 70(2), 524–541, https://doi.org/10.1175/JAS-D-11-0340.1.

Han, J., M. Witek, J. Teixeira, R. Sun, H. Pan, J. Fletcher, and C. Bretherton, 2016: Implementation in the NCEP GFS of a Hybrid Eddy-Diffusivity Mass-Flux (EDMF) Boundary Layer Parameterization with Dissipative Heating and Modified Stable Boundary Layer Mixing. Weather and Forecasting, 2016, 31:341–352, https://doi.org/10.1175/WAF-D-15-0053.1.

Hong, S. Y., Y. Noh, J. Dudhia, 2006: A new vertical diffusion package with an explicit treatment of entrainment processes. Mon. Wea. Rev. , 134(9), 2318–2341, https://doi.org/10.1175/MWR3199.1.

Huang, Q., X. Zhang, X. Zhu, Y. Zhu, and Y. Yang, 2025: The impact of the representation of in-cloud mixing effect in the planetary boundary layer scheme on the simulated track of tropical cyclone Infa (2021). Atmos. Res., 326, 108274, https://doi.org/10.1016/j.atmosres.2025.108274.

Iacono, M. J., J. S. Delamere, E. J. Mlawer, M. W. Shephard, S. A. clough, and W. D. Collins, 2008: Radiative forcing by long-lived greenhouse gases: Calculations with the AER radiative transfer models. J. Geophys. Res. Atmos., 113(D13), https://doi.org/10.1029/2008JD009944.

Kepert, J. D., 2001: The dynamics of boundary layer jets within the tropical cyclone core. Part I: Linear theory. J. Atmos. Sci., 58, 2469–2484, https://doi.org/10.1175/1520-0469(2001)058<2469:TDOBLJ>2.0.CO;2.

Kepert, J. D., 2012: Choosing a boundary layer parameterization for tropical cyclone modeling. Mon. Wea. Rev., 140, 1427–1445, https://doi.org/10.1175/MWR-D-11-00217.1.

Li, X., Y. Zhang, X. Peng, W. Chu, Y. Lin, and J. Li, 2022: Improved climate simulation by using a double-plume convection scheme in a global model. J. Geophys. Res. Atmos., 127(11): e2021JD036069. https://doi.org/10.1029/2021JD036069.

Li, X., Y. Zhang, Y. Lin, X. Peng, B. Zhou, P. Zhai and J. Li, 2023: Impact of revised trigger and closure of the double-plume convective parameterization on precipitation simulations over east Asia. Adv. Atmos. Sci., 40(7): 1225−1243, https://doi.org/10.1007/s00376-022-2225-9.

Li, Y., Y. Tang, S. Wang, R. Toumi, X. Song, and Q. Wang, 2023: Recent increases in tropical cyclone rapid intensification events in global offshore regions. Nat. Commun. 14, 5167, https://doi.org/10.1038/s41467-023-40605-2.

Liu, K. S., and J. C. L. Chan, 2022: Growing threat of rapidly-intensifying tropical cyclones in East Asia. Adv. Atmos. Sci. 39, 222–234, https://doi.org/10.1007/s00376-021-1126-7.

Lorsolo, S., J. L. Schroeder, P. Dodge, and F. Marks Jr., 2008: An observational study of hurricane boundary layer small-scale coherent structures. Mon. Wea. Rev., 136, 2871–2893, https://doi.org/10.1175/2008MWR2273.1.

Louis, J.F., 1979. A parametric model of vertical eddy fluxes in the atmosphere. Bound. Layer Meteorol. 17, 187–202. https://doi.org/10.1007/BF00117978.

Ming, J., and J. A. Zhang, 2016: Effects of surface flux parameterization on the numerically simulated intensity and structure of Typhoon Morakot (2009). Adv. Atmos. Sci., 33, 58–72, https://doi.org/10.1007/s00376-015-4202-z.

Montgomery, M. T., and R. K. Smith, 2014: Paradigms for tropical cyclone intensification. Australian Meteorological and Oceanographic Journal, 64 37–66, https://doi.org/10.22499/2.6401.005.

Montgomery, M. T., R. K. Smith, and S. Nguyen, 2010: Sensitivity of tropical cyclone models to the surface drag coefficient. Quart. J. Roy. Meteor. Soc., 136, 1945–1953, https://doi.org/10.1002/qj.702.

Montgomery, M. T., G. Kilroy, R. K. Smith, and N. ˇCrnivec, 2020: Contribution of eddy momentum processes to tropical cyclone intensification. Quart. J. Roy. Meteor. Soc.,146, 3101–3117, https://doi.org/10.1002/qj.3837.

O'Brien, J. J., 1970: A note on the vertical structure of the eddy exchange coefficient in the planetary boundary layer. J. Atmos. Sci., 27, 1213–1215, https://doi.org/10.1175/1520-0469(1970)027<1213:ANOTVS>2.0.CO;2.

Ooyama, K. V., 1969: Numerical simulation of the life cycle of tropical cyclones. J. Atmos. Sci., 26, 3–40, https://doi.org/10.1175/15200469(1969)026%3C0003:NSOTLC%3E2.0.CO;2.

Powell, M. D., P. J. Vickery, and T. A. Reinhold, 2003: Reduced drag coefficient for high wind speeds in tropical cyclones. Nature, 422, 279–283, https://doi.org/10.1038/nature01481.

Smith, R. K., and M. T. Montgomery, 2010: Hurricane boundary layer theory. Quart. J. Roy. Meteor. Soc., 136A, 1665–1670, https://doi.org/10.1002/qj.679.

Smith, R. K., M. T. Montgomery, and S. V. Nguyen, 2009: Tropical cyclone spin-up revisited. Quart. J. Roy. Meteor. Soc., 135, 1321–1335, https://doi.org/10.1002/qj.428.

Song, J., Y. Duan, and P. J. Klotzbach, 2020: Increasing trend in rapid intensification magnitude of tropical cyclones over the western North Pacific. Environ. Res. Lett. 15, 084043, https://doi.org/10.1088/1748-9326/ab9140.

Tallapragada, V., C. Kieu, Y. Kwon, S. Trahan, Q. Liu, Z. Zhang, and I. Kwon, 2014: Evaluation of storm structure from the operational HWRF model during 2012 implementation. Mon. Wea. Rev. , 142(11), 4308–4325, https://doi.org/10.1175/MWR-D-13-00010.1.

Troen, I. B., & Mahrt, L. (1986). A simple model of the atmospheric boundary layer; sensitivity to surface evaporation. Boundary-Layer Meteorology, 37(1), 129–148. https://doi.org/10.1007/BF00122760.

Vogelezang, D. H. P., and A. A. M. Holtslag, 1996: Evaluation and model impacts of alternative boundary-layer height formulations. Boundary-Layer Meteorology, 81(3), 245–269. https://doi.org/10.1007/BF02430331.

Xu, K. M., and D. A. Randall, 1996: A semiempirical cloudiness parameterization for use in climate models. J. Atmos. Sci., 53(21), 3084–3102, https://doi.org/10.1175/1520-0469(1996)053<3084:ASCPFU>2.0.CO;2

Zhang, J. A., and F. D. Marks, M. T. Montgomery, and S. Lorsolo, 2011: An estimation of turbulent characteristics in the low-level region of intense Hurricanes Allen (1980) and Hugo (1989). Mon. Wea. Rev., 139, 1447–1462, https://doi.org/10.1175/2010MWR3435.1.

Zhang, J. A., and W. M. Drennan, 2012: An observational study of vertical eddy diffusivity in the hurricane boundary layer. J. Atmos. Sci., 69, 3223–3236, https://doi.org/10.1175/JAS-D-11-0348.1.

Zhang, J. A., and R. T. Rogers, 2019: Effects of Parameterized Boundary Layer Structure on Hurricane Rapid Intensification in Shear. Mon. Wea. Rev., 147, 853–871, https://doi.org/10.1175/MWR-D-18-0010.1.

623 Zhang, J. A., D. S. Nolan, R. F. Rogers, and V. Tallapragada, 2015: Evaluating the impact of
624 improvements in the boundary layer parameterization on hurricane intensity and structure
625 forecasts in HWRF. Mon. Wea. Rev., 143, 3136–3155, https://doi.org/10.1175/MWR-D-14-
626 00339.1.
627 Zhang, J. A., R. F. Rogers, and V. Tallapragada, 2017: Impact of parameterized boundary layer
628 structure on tropical cyclone rapid intensification forecasts in HWRF. Mon. Wea. Rev., 145,
629 1413–1426, https://doi.org/10.1175/MWR-D-16-0129.1.
630 Zhang, Y., J. Li, R. Yu, et al. 2020. A multiscale dynamical model in a dry-mass coordinate for
631 weather and climate modeling: Moist dynamics and its coupling to physics. Mon. Wea. Rev.,
632 148(7): 2671−2699, https://doi.org/10.1175/mwr-d-19-0305.1.
633 Zhang, Y., X. Li, Z. Liu, X. Rong, J. Lin, Y. Zhou, and S. Chen, 2022: Resolution
634 sensitivity of the GRIST nonhydrostatic model from 120 to 5 km (3.75 km)
635 during the DYAMOND winter. Earth and Space Science, 9(9): e2022EA002401,
636 https://doi.org/10.1029/2022EA002401.
637 Zhang, Y., J. Li, R. Yu, S. Zhang, Z. Liu, J. Huang, and Y. Zhou, 2019: A layer-averaged
638 nonhydrostatic dynamical framework on an unstructured mesh for global and regional
639 atmospheric modeling: Model description, baseline evaluation, and sensitivity exploration. J.
640 Adv. Model. Earth Syst., 11(6): 1685−1714, https://doi.org/10.1029/2018MS001539.
641 Zhang. Y, R. Yu, J. Li, X. Li, X. Rong, X. Peng, and Y. Zhou, 2021: AMIP simulations of a global
642 model for unified weather–climate forecast: Understanding precipitation characteristics and
643 sensitivity over East Asia. J. Adv. Model. Earth Syst., 13(11): e2021MS002592,
644 https://doi.org/10.1029/2021MS002592.
645 Zhao, H., X. Duan, G. B. Raga, and P. J. Klotzbach, 2018: Changes in characteristics of rapidly
646 intensifying Western North Pacific tropical cyclones related to climate regime shifts. J. Clim.
647 31, 8163–8179, https://doi.org/10.1175/jcli-d-18-0029.1.